Modeling of the two-phase flow during depressurization of liquified CO_2 in a pipe

Osama M Ibrahim[a,*], Prasanna Welahettige [a], Knut Vågsæther [a], Bernt Lie [a]

[a] *The University of South-Eastern Norway, Faculty of Technology, Natural Sciences, and Maritime Sciences, Kjølnes Ring 56, 3918 Porsgrunn, Norway*

Osama.K.Ibrahim@usn.no

Abstract

Modeling transient CO_2 two-phase flow in a pipe is essential in studying depressurization mechanisms resulting from liquified CO_2 accidental release. Generated data from such models predict the released flow characteristics and possible propagating fractures. Accordingly, they provide valuable input for risk prevention in designing and safely operating CO_2 transport pipelines. CO_2 depressurization simulation involves fluid-mechanical and thermodynamic models, primarily expressed by hyperbolic partial differential equations and an equation of state (EOS). Besides, these models are solved with appropriate numerical methods. This paper deals with a drift flux - homogeneous equilibrium model (HEM) construction utilizing central-upwind-weighted essentially non-oscillatory (WENO) numerical schemes to describe two-phase flow during CO_2 decompression in a pipe. Rapid transition in mass, momentum, and energy at the interface between liquid and vapor phases is assumed in the flow HEM. Thus, the two-phase flow is in a thermal, mechanical, and chemical equilibrium. The thermodynamic properties are calculated by applying Span-Wagner EOS. The high-resolution second-order central, central-upwind, and third-order weighted essentially non-oscillatory (WENO) schemes have been executed with the HEM, and they effectively captured rapid phase transition. The central-upwind and essentially non-oscillatory (ENO) schemes' stencils can be appropriate for constructing a higher-order accuracy central-upwind-WENO scheme. This structured scheme uses a smoothness indicator as an alternative to the limiter function. Besides, the variables in the cell interface are determined by WENO reconstruction, while central-upwind is used to compute the flux properties.

1. Introduction

As long as fossil fuel is the predominant energy source, carbon capture and storage (CCS) technology should be critical to reducing greenhouse gas. CCS is projected to contribute more than 20% to CO_2 emissions reduction by 2050, as reported by the International Energy Agency (IEA) [1]. That means above nine gigatons should be captured and stored every year. Safe and consistent carbon dioxide (CO_2) transport from capturing plants to storage sites is vital in the CCS process. On- and offshore pipelines represent a favorable option for transporting large quantities of CO_2. However, this process raises growing safety concerns as CO_2 is transported in a high pressurized dense phase and involves a significant hazard of pipe failure. Pipelines can endanger running-ductile fracture from expansion and explosive evaporation waves following the rapid phase transition during liquid CO_2 depressurization [2]. Subsequently, the pipe may expose to destructive damage due to the fast reduction in temperature during the evaporation process. Therefore, estimating the thermodynamic state properties during the decompression process is crucial for the appropriate design, safe operation, and maintenance of CO_2 transport pipes. For this purpose, transient flow models are required, whereby fluid-mechanical and thermodynamic models are coupled with appropriate numerical methods to resolve these models. These models should be validated and corrected by experimental data.

The CO_2 pipe's mechanical failure potentially results in a release of two-phase flow, following isentropic expansion due to pressure decrease. The intensity and propagation velocity of downstream two-phase flow depends on the upstream expansion waves' velocity traveling into superheated liquid. Thus, estimating the change in velocities along the pipe is essential to predict the release behavior and the pipe fracture development. Several models have been used to predict state properties during pure or CO_2-rich mixtures depressurization. Elshahomi et al. [3] have predicted CO_2 state properties during condensation phase transition using ANSYS Fluent, CFD procedure. The results had good agreement

with previous shock tube experimental data. Munkejord et al. [4, 5] have applied two models to study the influence of impurities and the initial temperature on wave velocity during CO_2-rich mixture decompression. The homogeneous equilibrium model (HEM) and the two-fluid model (TFM) were formulated by implementing the multi-stage centered scheme (MUSTA) simultaneously with Soave-Redlich-Kwong and Peng-Robinson EOS to calculate the thermodynamical properties. The models' calculation findings were contrasted with shock tube test results, which demonstrated minimal enhancement in TFM predictions against HEM. Botros et al. [6] have performed shock tube experiments on pure CO_2 and compared the results with estimations from models built on three equations of state: GERG-2008, Peng-Robinson, and BWRS. They concluded that only GERG-2008 corresponded with experimental data. However, the inconsistency increased with temperature reduction. Morin et al. [7] have presented an approximate Riemann solver of Roe for the pipe's CO_2 depressurization. Simulation results demonstrated that the central scheme underestimated the pressure pulse's maximum amplitude. While the high-resolution Roe scheme accurately described the pulse. A homogeneous relaxation model (HRM) with cubic EOS was introduced by Brown et al. [8] to describe the released flow resulting from dense phase CO_2 pipe rupturing. The model was resolved by conjugating a semi-discrete Finite Volume Method and HLL (Harten-Lax-van Leer) approximate Riemann solver. It also showed reasonable agreement with the real data from rupturing the CO_2 pipeline. In this paper a drift flux - (HEM) is built utilizing central-upwind-weighted essentially non-oscillatory (WENO) numerical schemes to illustrate two-phase flow following CO_2 decompression in a pipe.

2. Methodology

This model incorporates the drift-flux model (homogeneous equilibrium), Span-Wagner Equation of State, and centered-upwind-WENO scheme, including the Runge-Kutta fourth-order method to describe the transients' characteristics during liquid CO_2 decompression. The model illustrates one component (CO_2) with two-phase flow inside a horizontal pipe and is assumed to be in thermal, mechanical, and chemical equilibrium. i.e., the gas and liquid phases have the same temperature (T), pressure (P), and chemical potential (μ).

$$T_l = T_g = T; \quad P_l = P_g = P; \quad \mu_l = \mu_g = \mu \qquad (1)$$

2.1. Fluid dynamics in the pipe flow model

Unlike the Drift Flux Model (DFM) in the HEM model, the gas and liquid velocity are identical (no slip). In addition, the model is one-dimensional due to flow in one direction along the pipe. The flow variables are averaged over the pipe's cross-section. The governing equations are in the form of hyperbolic partial differential equations similar to Euler's equations for compressible inviscid flow of a single fluid and can be described as

$$\frac{\partial}{\partial t}U + \frac{\partial}{\partial x}F = 0 \qquad (2)$$

where U is the vector that contains the conserved variables and $F(U)$ is the flux function:

$$U = [\rho, \rho v, E]; \;\; F = [\rho v, \rho v^2 + P, v(E+P)] \qquad (3)$$

Correlated closure laws for the HEM constitute the two-phase mixture density ρ, the total energy E, the corresponding mixture's specific internal energy e_{mix}, and the volume fraction relation as follows

$$\left.\begin{aligned} &\rho = \alpha_g \rho_g + \alpha_l \rho_l ; \\ &E = \rho(e + 0.5v^2); \\ &e = \left(\alpha_g \rho_g e_g + \alpha_l \rho_l \, e_l\right)/\rho; \\ &\alpha_g + \alpha_l = 1 \end{aligned}\right\} \qquad (4)$$

where ρ denotes density, v - velocity, E – the total energy, e – specific internal energy, P – pressure, α_i – volume fraction of the phase i, and subscripts g and l are gas and liquid phases, respectively. For simplicity, the source terms are not included, i.e., the heat transfer through the pipe wall, wall friction, and the gravitational forces are neglected. Equation (2) can be written in a quasi-linear form as :

$$U_t + A(U)U_x = 0 \qquad (5)$$

where $A(U) = \frac{\partial F}{\partial U}$ is the Jacobian matrix of the system.

2.2. Thermodynamics

A function $P(e, \rho)$ that relates the pressure to the internal energy and density is required to complete the model. This work uses the Span-Wagner Equation of State (SW EOS). It is considered the most accurate EOS for CO_2 and is based on Helmholtz's free energy (HFE) as a function of temperature, volume, and the number of moles: *A(T, V, N)*. The molar properties of the HFE and the volume are

$$a = \frac{A}{N}; \quad v = \frac{V}{N} \qquad (6)$$

It implies that $a(T, \mathcal{v})$. The relation of a to the other thermodynamic properties can be expressed in terms of partial derivatives of the independent variable $(T, \mathcal{v})$. The relation to the pressure, internal energy, and entropy are as follows:

$$\left.\begin{aligned} P &= -\frac{\partial a}{\partial \mathcal{v}}\ ; \\ e &= a + Ts = a - T\frac{\partial a}{\partial T}\ ; \\ s &= -\frac{\partial a}{\partial T}\ ; \end{aligned}\right\} \quad (7)$$

As the phase transition occurs following adiabatic pressure reduction, The molar entropy is conserved. The temperature is unknown, and it is required to solve one or more linear equations involving e and $\mathcal{v}$ to determine its value. SW EOS demonstrates explicit expressions for HFE's appropriate partial derivatives, allowing for numerically solving for the temperature using Newton's method. The initial molar volume and internal energy $(\mathcal{v}_0,\ e_0)$ can be determined as a function of the known initial saturated temperature and pressure (T_0, P_0). Then the equation involving molar internal energy as a function of temperature and molar volume should be solved by newton's method iteration

$$\begin{aligned} G(X) &= [e(X) - e_0] = 0; \\ X_{i+1} &= X_i - J^{-1} \cdot G(X) \end{aligned} \quad (8)$$

Here X signifies the vector $(T, \mathcal{v})^T$, and $J = \frac{\partial e}{\partial T}$ is the Jacobian of G. Then the thermodynamic state is determined as a function of T and $\mathcal{v}$ (Mjaavatten, 2022).

The speed of sound in the mixture is given as:

$$c_m = \sqrt{\frac{\mathcal{v}^2}{M_W} \cdot \left(\frac{\partial a^2}{\partial \mathcal{v}^2} - \frac{\partial a^2}{\partial \mathcal{v} \partial T}\right)} \quad (9)$$

In addition, $\rho = \frac{M_W}{\mathcal{v}}$; where M_W is the molecular weight (for CO_2, 44.01g/mol).

2.3. Numerical method

Equation (2) can be solved using the finite-volume scheme, wherein the domain is discretized into subdomains (control volumes). The semi-discrete formula (spatial operator discretization) can be obtained by Eq. (2) integration:

$$L(U) = -\frac{1}{\Delta x}\left(F_{i+\frac{1}{2}} - F_{i-\frac{1}{2}}\right) \quad (10)$$

where $L(U)$ - discretization of the spatial operator; $F_{i+\frac{1}{2}}$ - the flux between cells i and $i+1$. Time iteration for the semi-discrete formula is executed using the total variation diminishing (TVD) Runge-Kutta method (RKM). According to Gottlieb et al. (1998), this method keeps TVD properties satisfying the Courant-Friedrichs-Lewy (CFL) condition. The time iterations by fourth-order TVD RCM are expressed as (Shu and Osher, 1988) :

$$U^{(1)} = U^{(0)} + \tfrac{1}{2}\Delta t L(U); \quad (11.1)$$

$$U^{(2)} = \tfrac{1}{2}U^{(0)} + \tfrac{1}{2}U^{(1)} - \tfrac{1}{4}\Delta t L\left(U^{(0)}\right) + \tfrac{1}{2}\Delta t L\left(U^{(1)}\right); \quad (11.2)$$

$$U^{(3)} = \tfrac{1}{9}U^{(0)} + \tfrac{2}{9}U^{(1)} + \tfrac{2}{3}U^{(2)} - \tfrac{1}{9}\Delta t L\left(U^{(0)}\right) - \tfrac{1}{3}\Delta t L\left(U^{(1)}\right) + \Delta t L\left(U^{(2)}\right); \quad (11.3)$$

$$U^{(4)} = \tfrac{1}{3}U^{(1)} + \tfrac{1}{3}U^{(2)} + \tfrac{1}{3}U^{(3)} + \tfrac{1}{6}\Delta t L\left(U^{(1)}\right) + \tfrac{1}{6}\Delta t L\left(U^{(3)}\right) \quad (11.4)$$

where $U^{(0)}$ and $U^{(4)}$ are properties at the time *n* and *n+1*, respectively. Considering the CFL limitation, the time step is specified as:

$$\Delta t \le c \cdot (\Delta x / \max\{\lambda_i\}\ \forall i) \quad (12)$$

where c is the CFL number and λ_i are the eigenvalues of the Jacobian matrix: $A(U) = \frac{\partial F}{\partial U}$.

It is challenging to discretize precisely the cell interface flux function. i.e., The flux $F_{i+\frac{1}{2}}$ is challenging to determine at the cell interface given the values of U_i, U_{i+1}, $U_i{}^n$, and $U_i{}^{n+1}$. Many numerical approaches have been suggested to compute $F_{i+\frac{1}{2}}$. This work applies the centered-upwind-WENO scheme (CU-WENO), developed by (Welahettige et al., 2022), for the HEM to calculate the flux functions by the central-upwind scheme while the cell interface properties by WENO reconstruction. This formulation seeks to integrate the central-upwind features into the WENO scheme, which could improve the results' accuracy and stability.

The cell interface flux is computed according to the central-upwind expression presented by Kurganov et al. (2001). The scheme specifies the local speeds on the side of wave propagation's directions (discontinuity propagation speeds). Their values are equivalent to the maximum and minimum of the Jacobian matrix's eigenvalues. The positive and negative discontinuity propagation speeds are defined as

$$a_{i+\frac{1}{2}}^{n,+} = \max\left\{ \begin{matrix} \max\left\{\lambda\left(U_{i+\frac{1}{2}}^{n,-}\right)\right\}, \\ \max\left\{\lambda\left(U_{i+\frac{1}{2}}^{n,+}\right)\right\}, 0 \end{matrix} \right\} \quad (13.1)$$

$$a_{i+\frac{1}{2}}^{n,-} = \min\left\{ \begin{array}{l} \min\left\{\lambda\left(U_{i+\frac{1}{2}}^{n,-}\right)\right\}, \\ \min\left\{\lambda\left(U_{i+\frac{1}{2}}^{n,+}\right)\right\}, 0 \end{array} \right\} \quad (13.2)$$

where λ denotes the eigenvalues of HEM:

$$\lambda = \{v + c_m, v, v - c_m\} \quad (13.3)$$

Then, for the central-upwind scheme, the high-resolution numerical flux is expressed as:

$$F(U)_{i+\frac{1}{2}}^{n} = \frac{a_{i+\frac{1}{2}}^{n,+} \cdot F\left(U_{i+\frac{1}{2}}^{n,-}\right) - a_{i+\frac{1}{2}}^{n,-} \cdot F\left(U_{i+\frac{1}{2}}^{n,+}\right)}{a_{i+\frac{1}{2}}^{n,+} - a_{i+\frac{1}{2}}^{n,-}} - \frac{a_{i+\frac{1}{2}}^{n,+} \cdot a_{i+\frac{1}{2}}^{n,-}}{a_{i+\frac{1}{2}}^{n,+} - a_{i+\frac{1}{2}}^{n,-}} \cdot \left(U_{i+\frac{1}{2}}^{n,+} - U_{i+\frac{1}{2}}^{n,-}\right) \quad (14)$$

The cell interface properties are calculated by applying a fifth-order WENO reconstruction based on a third-order ENO stencils approach; for (r)-order ENO, (2r-1)-order WENO can be constructed. The cell averages calculate the cell interface properties in each stencil. So, the negative direction value at the cell interface $i + \frac{1}{2}$ is given as:

$$U_{i+\frac{1}{2}}^{-} = \omega_0 U_{i+\frac{1}{2}}^{-,0} + \omega_1 U_{i+\frac{1}{2}}^{-,1} + \omega_2 U_{i+\frac{1}{2}}^{-,2} \quad (15)$$

Here, ω is a weight function. The sum of weight functions is one ($\omega_0 + \omega_1 + \omega_2 = 1$), and they are calculated as:

$$\omega_0 = \frac{\alpha_0}{\alpha_0+\alpha_1+\alpha_2}; \omega_1 = \frac{\alpha_1}{\alpha_0+\alpha_1+\alpha_2}; \omega_2 = \frac{\alpha_2}{\alpha_0+\alpha_1+\alpha_2} \quad (16)$$

Where α_i are given as:

$$\alpha_0 = \frac{1}{10\cdot(\epsilon+\beta_0)^2}; \alpha_1 = \frac{6}{10\cdot(\epsilon+\beta_1)^2}; \alpha_2 = \frac{3}{10\cdot(\epsilon+\beta_2)^2} \quad (17)$$

Where setting $\epsilon = 10^{-6}$ aims to avoid division by zero. β - is a smoothness indicator that involves (r-1)-order polynomial function

$$\beta_0 = \frac{13}{12}(\mathrm{U}_{i-2} - 2\mathrm{U}_{i-1} + \mathrm{U}_i)^2 + \frac{1}{4}(\mathrm{U}_{i-2} - 4\mathrm{U}_{i-1} + 3\mathrm{U}_i)^2; \quad (18.1)$$

$$\beta_1 = \frac{13}{12}(\mathrm{U}_{i-1} - 2\mathrm{U}_i + \mathrm{U}_{i+1})^2 + \frac{1}{4}(\mathrm{U}_{i-1} - \mathrm{U}_{i+1})^2; \quad (18.2)$$

$$\beta_2 = \frac{13}{12}(\mathrm{U}_i - 2\mathrm{U}_{i+1} + \mathrm{U}_{i+2})^2 + \frac{1}{4}(3\mathrm{U}_i - 4\mathrm{U}_{i+1} + \mathrm{U}_{i+2})^2 \quad (18.3)$$

The positive direction value $U_{i+\frac{1}{2}}^{+}$ at the cell interface $i + \frac{1}{2}$ can be calculated by symmetry.

3. Results and discussions

Numerical simulations analyzing the transient pipe flow behavior during the evaporation of the CO_2 dense phase are presented. The CU-WENO numerical schemes resolve hyperbolic conservation equations. The fluid dynamics part is combined with SW EOS to determine the variations in thermodynamic properties. The release incident involves the decompression of liquified CO_2 in a pipe length of 100 m. The initial conditions are: pressure (P_0) = 7.27 MPa, temperature (T_0) = 303.5 K and velocity (v_0) = 0 m/s. The simulation sets out at x = 50 m, t = 0 s after the pipe end ruptures, and the liquid CO_2 depressurizes to a pressure of 3,67 MPa. As a result, a rarefaction wave travels through the liquid, causing its expansion to superheated liquid. Then, the evaporation wave moves through the superheated liquid, leading to its evaporation and generating an expanded two-phase mixture propagating toward the pipe's end with high velocity.

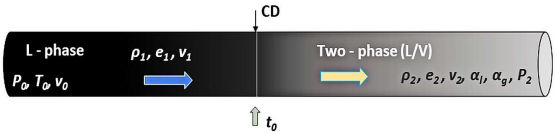

Figure 1: Schematic drawing shows CO_2 depressurization in a pipe.

Figure 2 shows the pressure, mixture velocity, and vapor/liquid volume fraction variations along the pipe's length. The plots demonstrate calculations for 1000 cells and 90 ms after the pipe ruptures. The passage of the rarefaction wave begins with the gradual liquid expansion corresponding to a pressure decrease from about 7.3 to 6.9 MPa and then a steep decline to almost 5.1MPa (Figure 2(a)). The expanded superheated liquid remains in a metastable state at nearly constant pressure (slightly convex route), passing about 12.6 m before the pressure decreases sharply, indicating rapid evaporation.

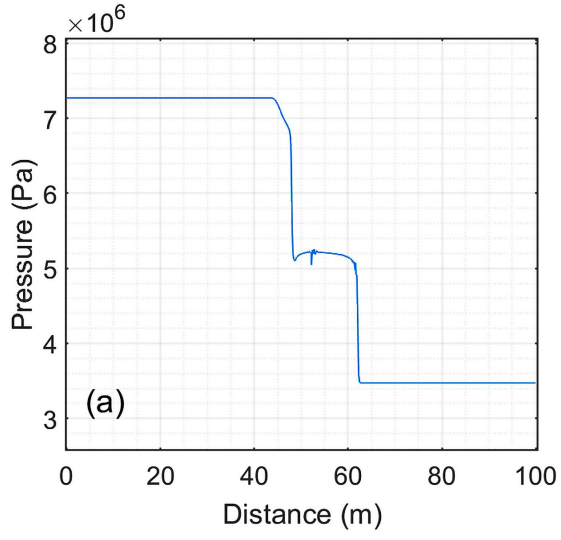

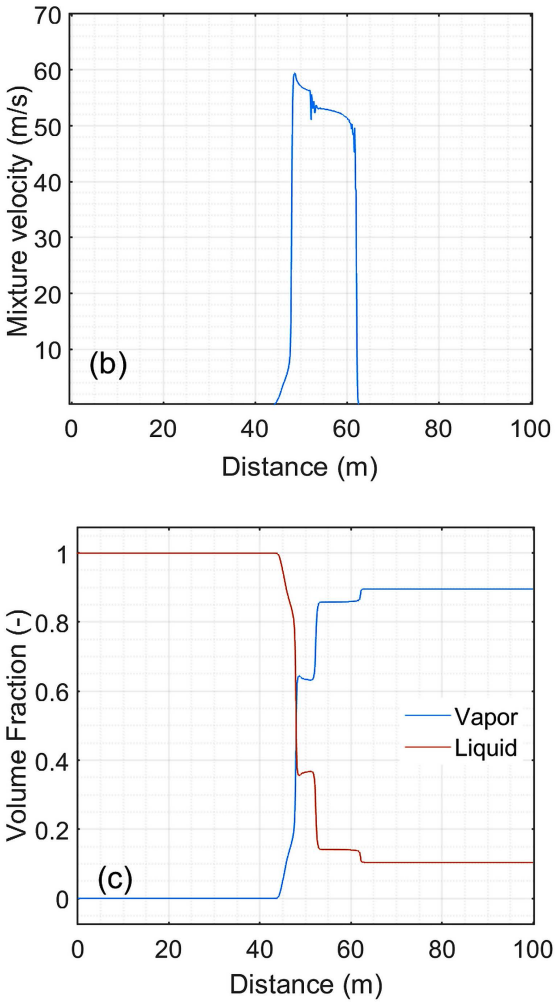

Figure 2: Change in pressure (a), mixture velocity (b), and vapor/liquid volume fraction (c) along the pipe's length during 90 ms of liquified CO_2 depressurization.

In addition, the rapid pressure drop results in the propagation of expanded fluid with increased velocity up to 59.3 m/s. Subsequently, the velocity decreases with small fluctuations before its abrupt drop once the evaporation wavefront has passed.

The vapor volume fraction (VVF) has risen in steps following the change in the thermodynamic state described by the pressure route. As seen in Figure 2 (c), complete evaporation has not been attained, and the third (last) jump in VVF seems to be related to the contact discontinuity wave.

Particular difficulties were encountered in the model implementation when depressurization was chosen to lower pressure near the atmospheric conditions. The temperature and subsequent calculated pressure showed unphysical behavior and may have been affected by the simplifying assumptions used in the model. In particular, the two-phase mixture velocity calculations can be vulnerable in contrast to the two-fluid model. The small rapid fluctuations seen in pressure and velocity profiles at about 52 and 61 m (Figure 2 (a) and (b)) are likely caused by numerical computation of the temperature as a function of molar internal energy and volume. The intermittent fluctuations sites corresponded with the beginning of the rapid change in the internal energy (see Figure 4 (c)), which may produce transient instability in temperature calculations.

Computations have been implemented on grid cells between 200 and 2000 to evaluate the convergence of the CU-WENO numerical schemes. An appropriate numerical method should not create additional unreal oscillations as the cells' number increases. Figure 3 illustrates the convergence results for mixture density (a) and pressure (b) after 60 ms, implementing various cells' numbers on the CU-WENO schemes. As seen in Figure 3, the solution converges well as the grid is refined, i.e., as the size of the cells shrinks.

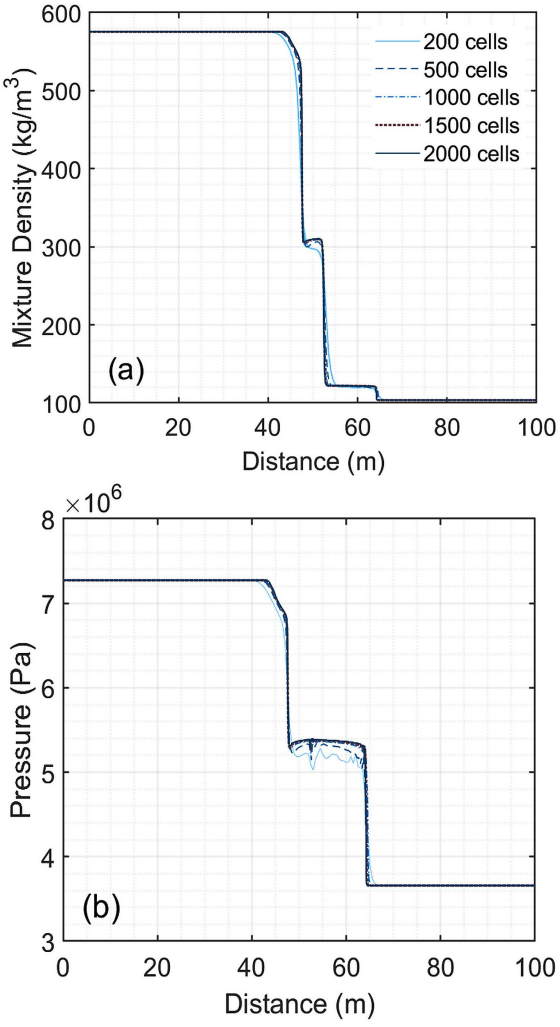

Figure 3: Grid refinement results for CU-WENO numerical schemes' convergence after 60 ms of CO_2 depressurization. (a) for mixture density, and (b) for the pressure.

There are no extra oscillations observed in either plot. Instead, the observed small fluctuations on the

pressure lines in Figure 3 (b) are flattened due to the grid refinement. The diffusivity of results reduces with grid refinement, and a grid size of 1500 can be recommended for the simulation.

Figure 4 shows vapor volume fraction (a), mixture density (b), and mixture internal energy (c) profiles along the pipe's length at different time stamps of 30, 50, 70, and 100 ms after the rupture. The waves' behavior can be described by tracing the changes in property profiles. The initial pressure gradient promotes the generation of three waves: shock and contact discontinuity, traveling in the right direction. Besides, an expansion wave moves in the opposite left direction.

In Figure 4 (a), the second and third sharp increases in VVF signifies the evaporation wavefront and the contact discontinuity, respectively. Additionally, the evaporation wavefront propagates towards the left as time runs, while the shock and contact surface propagate in the right direction.

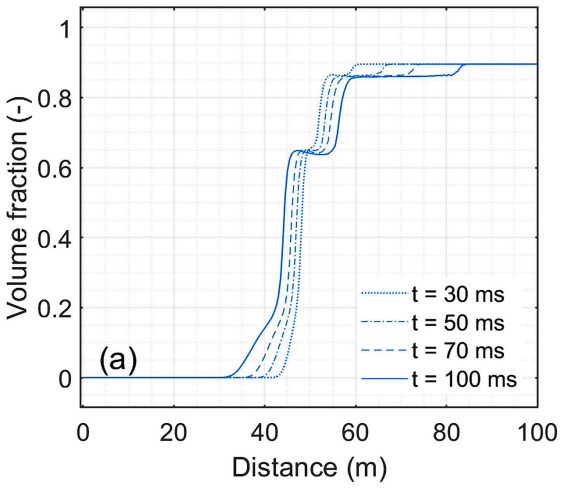

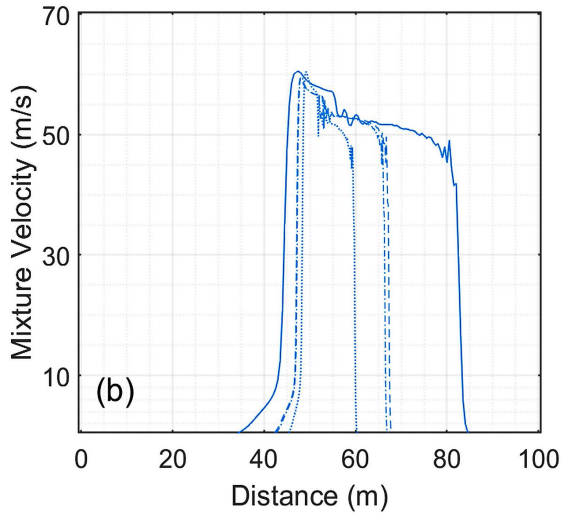

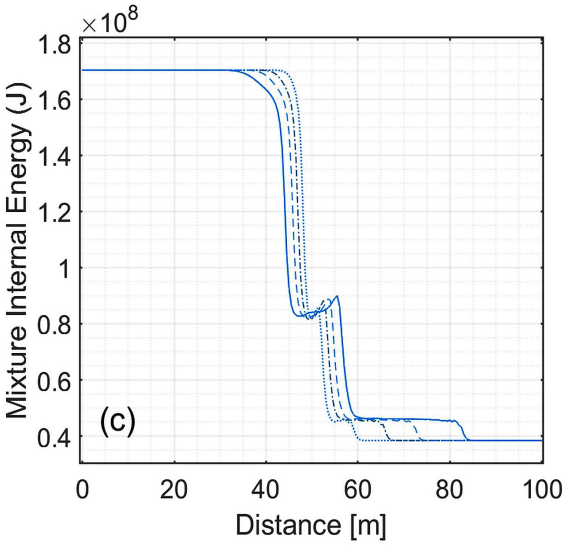

Figure 4: The behavior of vapor volume fraction (a), mixture density (b), and mixture internal energy (c) along the pipe's length during various time intervals and for 1000 grid cells.

The velocity profile in Figure 4 (b) demonstrates the two-phase mixture movement along the pipe towards the vented end. At the same time, the velocity peak increases while it moves in the reverse direction. However, the pressure wave behavior affects the two-phase mixture velocity after the evaporation starts due to the expansion waves' sequence propagation with different speeds (see Figure 4 (b) and Figure 2 (b)).

Figure 4 (c) shows that the mixture's internal energy rises in the metastable state following the rarefaction wave. This trend could be attributed to the liquid state transition from saturated to superheated, whereby the liquid stores the gained energy during its expansion as long as it remains in the metastable state. Then the energy is released during the phase change process providing the required latent heat of vaporization.

4. Conclusions

Then the energy A homogeneous equilibrium model (HEM) for two-phase flow during CO_2 depressurization in a pipe has been developed. The model considers equilibrium in pressure, temperature, and chemical potential, using SW EOS to calculate fluid properties in different thermodynamic states. Additionally, the method integrates two numerical schemes to use the CU-WENO scheme, wherein the numerical flux is calculated from central-upwind flux and the cell interface values from the third-order WENO reconstruction. The aim is to fit the central-upwind features in the WENO scheme, which can enhance accuracy and stability. The model is able to trace the

pressure, two-phase mixture density, and vapor volume fraction patterns during the rapid phase transition. In addition, the simulation results demonstrate the model's ability to predict the rarefaction and evaporation waves' dynamic characteristics and the convergence of the CU-WENO scheme. The numerical method well captured the moving discontinuity without blurs, and they have a similar pattern as in works done, for instance, by Munkejord et al. (2010) and Morin et al. (2010). However, the CU-WENO scheme illustrated the shock and expansion waves with less sharp edge transitions compared to the mentioned studies.

It is important to mention that the presented model does not consider the slip between phases during the compression and describes it as a uniform mixture pattern inside the pipe. However, the pipe rupture could result in a stratified flow pattern whereby the phase slip velocities should be considered. Additionally, the choice of initial pressure is dictated by the depressurization model's characteristics, as good predictions have been achieved close to the critical point. Further study may consider the mentioned remarks in developing pipe CO_2 accidental release models.

References

Aursand E. *et al.* (2016) 'Fracture propagation control in CO_2 pipelines: Validation of a coupled fluid-structure model', *Engineering Structures*, vol. 123, pp. 192-212, doi: 10.1016/j.engstruct.2016.05.012.

Botros K. *et al.* (2015) 'Measurements of Decompression Wave Speed in Pure Carbon Dioxide and Comparison With Predictions by Equation of State' *Journal of Pressure Vessel Technology*, vol. 138, no. 3, doi: 10.1115/1.4031941.

Brown S. *et al.* (2013) 'A homogeneous relaxation flow model for the full bore rupture of dense phase CO_2 pipelines', *International Journal of Greenhouse Gas Control*, vol. 17, pp. 349-356, doi: 10.1016/j.ijggc.2013.05.020.

Elshahomi A *et al.* (2015) 'Decompression wave speed in CO_2 mixtures: CFD modelling with the GERG-2008 equation of state', *Applied Energy*, vol. 140, pp. 20-32, doi: 10.1016/j.apenergy.2014.11.054.

Gottlieb S. and Shu C.W. (1998) 'Total variation diminishing Runge-Kutta schemes' *Mathematics of Computation*, vol. 67, no. 221, pp. 73–85, doi: 10.1090/S0025-5718-98-00913-2.

Kurganov A., Noelle S., and Petrova G.(2001) 'Semidiscrete Central-Upwind Schemes for Hyperbolic Conservation Laws and Hamilton--Jacobi Equations SIAM' *Journal on Scientific Computing*, vol. 23, no. 3, pp. 707-740, doi: 10.1137/S1064827500373413.

Mjaavatten A. (2022) 'thermodynamic models and tools for H_20, H_2, CO_2, and Air', https://github.com/aremj/thermodynamics/releases/tag/v2.1, GitHub.

Morin A. *et al.* (2010) 'Numerical Resolution of CO2 Transport Dynamics', *Proceedings of the 2009 SIAM Conference on "Mathematics for Industry" The Art of Mathematics for Industry (MI)*, doi:10.1137/1.9781611973303.13

Munkejord S. *et al.* (2010) 'Thermo- and fluid-dynamical modelling of two-phase multi-component carbon dioxide mixtures' *International Journal of Greenhouse Gas Control*, vol. 4, no. 4, pp. 589-596, doi: 10.1016/j.ijggc.2010.02.003.

Munkejord S. T. and Hammer M. (2015) 'Depressurization of CO_2-rich mixtures in pipes: Two-phase flow modelling and comparison with experiments' *International Journal of Greenhouse Gas Control*, vol. 37, pp. 398-411, doi: 10.1016/j.ijggc.2015.03.029.

Shu C.-W. and Osher S. (1988) 'Efficient implementation of essentially non-oscillatory shock-capturing schemes' *Journal of Computational Physics*, vol. 77, no. 2, pp. 439-471, doi: 10.1016/0021-9991(88)90177-5.

Welahettige P. *et al.* (2022) 'Development of central-upwind-WENO scheme for two-phase 1-D drift flux model in pipe flow', Submitted to the 63rd Conference on Simulation and Modelling (63rd SIMS),.